Lateral and longitudinal compaction of PRC1 overlap zones drives stabilization of interzonal microtubules

Carline Fermino do Rosário[a,b], Ying Zhang[a], Jennifer Stadnicki[a,b], Jennifer L. Ross[c], and Patricia Wadsworth[a,b,*]

[a]Department of Biology, and [b]Program in Molecular and Cellular Biology, University of Massachusetts Amherst, Amherst MA 01003; [c]Department of Physics, Syracuse University, Syracuse NY 13244

ABSTRACT **During anaphase, antiparallel–overlapping midzone microtubules elongate and form bundles, contributing to chromosome segregation and the location of contractile ring formation. Midzone microtubules are dynamic in early but not late anaphase; however, the kinetics and mechanisms of stabilization are incompletely understood. Using photoactivation of cells expressing PA-EGFP-α-tubulin we find that immediately after anaphase onset, a single highly dynamic population of midzone microtubules is present; as anaphase progresses, both dynamic and stable populations of midzone microtubules coexist. By mid-cytokinesis, only static, non-dynamic microtubules are detected. The velocity of microtubule sliding also decreases as anaphase progresses, becoming undetectable by late anaphase. Following depletion of PRC1, midzone microtubules remain highly dynamic in anaphase and fail to form static arrays in telophase despite furrowing. Cells depleted of Kif4a contain elongated PRC1 overlap zones and fail to form static arrays in telophase. Cells blocked in cytokinesis form short PRC1 overlap zones that do not coalesce laterally; these cells also fail to form static arrays in telophase. Together, our results demonstrate that dynamic turnover and sliding of midzone microtubules is gradually reduced during anaphase and that the final transition to a static array in telophase requires both lateral and longitudinal compaction of PRC1 containing overlap zones.**

Monitoring Editor
Sarah Wignall
Northwestern University

Received: Feb 7, 2023
Revised: Jun 20, 2023
Accepted: Jul 4, 2023

INTRODUCTION

Chromosome segregation during mitosis is accomplished by the bipolar mitotic spindle, which is comprised of microtubules and numerous structural and regulatory proteins (Glotzer, 2009; McIntosh, 2017; Vukušić *et al.*, 2019). A defining characteristic of the mitotic spindle is its dynamic nature. As cells enter mitosis, the nucleation and turnover of microtubules both increase (Heald & Khodjakov, 2015; Khodjakov & Rieder, 1999; Rusan *et al.*, 2001) and this dynamic behavior plays crucial roles in chromosome capture, alignment at the metaphase plate, spindle positioning in the cell, and chromosome segregation during anaphase (Grill *et al.*, 2003; Grill & Hyman, 2005; Stumpff *et al.*, 2012; Maiato *et al.*, 2017; Steblyanko *et al.*, 2020). In cultured mammalian cells, chromosome segregation in anaphase is accomplished as kinetochore fibers shorten, moving chromosomes closer to the spindle poles (anaphase A) and by spindle elongation (anaphase B) which is accompanied by elongation of overlapping–antiparallel midzone microtubules (Maiato & Lince-Faria, 2010; Roostalu *et al.*, 2010; Brust-Mascher & Scholey, 2011; McIntosh *et al.*, 2012; Vukušić & Tolić, 2021). Midzone microtubules, also called bridging fibers, are nucleated in the half spindle in an augmin-dependent manner and link sister kinetochore fibers, contributing to both chromosome alignment and segregation (Uehara *et al.*, 2009; Jagrić *et al.*, 2021; Štimac *et al.*, 2022). How midzone

This article was published online ahead of print in MBoC in Press (http://www.molbiolcell.org/cgi/doi/10.1091/mbc.E23-02-0049) on July 19, 2023.

Author contributions: P.W. and J.R. conceived of the project. C.F.d.R., P.W. and J.S. performed the experiments. Y.Z. performed initial photoactivation experiments. C.F.d.R. and J. S. performed data analysis. C.F.d.R. and P.W. assembled the figures. P.W., C.F.d.R. wrote the manuscript with assistance from J.S. and J.L.R.

*Address correspondence to: Patricia Wadsworth (patw@umass.edu).

Abbreviations used: CLASP1, cytoplasmic linker associated protein 1; CPC, chromosomal passenger complex; EM, electron microscopy; Kif4a, kinesin family member 4A; MKLP1, mitotic kinesin-like protein 1; PA-EGFP, photoactivatable enhanced green fluorescent protein; PRC1, protein regulator of cytokinesis 1.

microtubules contribute to force generation in anaphase varies in different cell types (Vukušić & Tolić, 2021). For example, in meiotic spindles, midzone microtubules generate pushing forces that drive chromosome segregation (Laband *et al*., 2017). The contribution of midzone-microtubule polymerization and sliding has also been documented in yeast and diatom spindles (Cande & McDonald, 1985; Khodjakov *et al*., 2004; Janson *et al*., 2007; Vukušić & Tolić, 2021). In cultured mammalian cells, force generation by the midzone changes over time, with pushing forces seen in early and braking forces in later anaphase (Saunders *et al*., 2007; Collins *et al*., 2014; Vukušić *et al*., 2017; Pamula *et al*., 2019; Yu *et al*., 2019). In some cell types, interactions of astral microtubules with cortical force generators also contribute to spindle elongation in anaphase (Aist *et al*., 1991, 1993; Kotak *et al*., 2014).

In addition to contributing to chromosome segregation, midzone microtubules play a well-established role in specification of the location of contractile ring formation (Cao & Wang, 1996; Wheatley, 1996; Alsop & Zhang, 2003, 2004). Several protein complexes, including the chromosome passenger complex (CPC) and centralspindlin, accumulate on midzone and equatorial astral microtubules and generate signals that activate the GTPase RhoA at the equatorial cell cortex (Jantsch-Plunger *et al*., 2000; Hirose *et al*., 2001; Mollinari *et al*., 2002; Nishimura & Yonemura, 2006; Canman *et al*., 2008; Hutterer *et al*., 2009; Adriaans *et al*., 2019). RhoA in turn activates formins and myosin to promote contractile ring formation and constriction (Li & Higgs, 2003; Matsumura, 2005).

A key component of midzone formation and function is the conserved antiparallel microtubule crosslinking protein, PRC1 (Mollinari *et al*., 2002; Kurasawa *et al*., 2004; Vernì *et al*., 2004; Zhu & Jiang, 2005). Mammalian cells lacking PRC1 fail to generate robust midzone arrays and frequently fail cytokinesis (Kurasawa *et al*., 2004; Mollinari *et al*., 2005; Adriaans *et al*., 2019). PRC1 interacts with several midzone components, including the microtubule plus-TIP binding protein CLASP1 which promotes microtubule growth (Liu *et al*., 2009; Al-Bassam *et al*., 2010; Maton *et al*., 2015; Aher *et al*., 2018). PRC1 also interacts with the centralspindlin subunit MKLP1 – an interaction which contributes to the mechanical properties of the midzone (Hutterer *et al*., 2009; Lee *et al*., 2015; Mishima & Lee, 2015). PRC1 regulates midzone length by recruiting the kinesin Kif4a, which suppresses the elongation of midzone microtubule plus-ends (Hu *et al*., 2011; Nunes Bastos *et al*., 2013; Subramanian *et al*., 2013). Live cell imaging of tagged PRC1 further shows that as anaphase progresses, PRC1 intensity increases and dynamic turnover decreases (Pamula *et al*., 2019; Asthana *et al*., 2021). The change in the extent of microtubule overlap measured in live cells expressing fluorescent PRC1 (Pamula *et al*., 2019; Asthana *et al*., 2021) confirms earlier results obtained by electron microscopy (EM; Mastronarde *et al*., 1993).

In vitro experiments with purified proteins provide additional insight into how PRC1 and Kif4a regulate antiparallel-microtubule dynamics. On individual microtubules PRC1 and Kif4a accumulate forming dynamic end tags; the length of the tag is proportional to PRC1 concentration and microtubule length (Subramanian *et al*., 2010, 2013). Mixtures of PRC1, Kif4a, and microtubules also form antiparallel bundles in vitro (Kapitein *et al*., 2008; Bieling *et al*., 2010; Wijeratne & Subramanian, 2018; Hannabuss *et al*., 2019). Microtubule overlap zones shorten as microtubules slide apart and eventually reach steady state; and overlap length is similar to the length of midzone overlap zones observed in cells (Bieling *et al*., 2010; Hannabuss *et al*., 2019). PRC1 has been shown to generate frictional forces to resist microtubule sliding, consistent with the braking function of midzones observed in cells (Aist *et al*., 1991, 1993; Saunders *et al*., 2007; Pamula *et al*., 2019; Gaska *et al*., 2020;). Modeling shows that microtubule sliding results in condensed regions of PRC1 near microtubule plus-ends (Hannabuss *et al*., 2019).

Despite information about the dynamics and distribution of PRC1 in midzones, the dynamic behavior of the microtubules to which PRC1, and other midzone proteins, are bound has not been systematically measured throughout anaphase. Here we report the results of experiments in live cells showing that midzone microtubules initially comprise a single population of highly dynamic microtubules and subsequently transition to a mixture of dynamic and more stable microtubules. By the time midcytokinesis is reached, these microtubules convert into a static array where no detectable turnover/dissipation can be observed. As the antiparallel-overlap length decreases, there is a corresponding change in the rate of microtubule sliding from early anaphase to late anaphase. Conversion to a static array occurs when highly compacted zones of PRC1 are measured in cells. Prevention of lateral compaction, by blocking cytokinesis, or longitudinal compaction by depletion of Kif4a or PRC1, results in midzone microtubule arrays that fail to form static arrays in telophase.

RESULTS

Gradual reduction in midzone microtubule turnover and sliding in anaphase

To understand microtubule dynamics throughout anaphase, we first quantified chromosome and pole motion during anaphase in LLC-Pk1 pig epithelial cells expressing EGFP-α-tubulin. Consistent with prior work in these cells, chromosomes move closer to the spindle poles as kinetochore fibers shorten (anaphase A) and simultaneously the distance between the spindle poles increases as midzone microtubules elongate (anaphase B; Figure 1A; Rusan & Wadsworth, 2005; Collins *et al*., 2014). The rate of chromosome motion is faster within the first minute after anaphase onset (AO) and gradually slows after 5 min (avg. rates of 2.4 and 1 μm/min, respectively). Similarly, the rate of pole-to-pole separation is rapid within the first minute and decreases after 5 min (avg. rates of 1.8 and 0.5 μm/min, respectively). To quantify midzone microtubule dynamics throughout anaphase, we photoactivated cells stably expressing PA-EGFP-α-tubulin and quantified the dissipation of fluorescence and the position of the marked region (Figure 1B; Tulu *et al*., 2003, 2010). To quantify fluorescence dissipation, an area was drawn around the activated region (Figure 1B, top). To determine the turnover half time, the fluorescence values were fitted to an exponential decay curve (Figure 1B, bottom left; see *Methods*). To quantify the sliding rate, the length of the activated region was measured (Figure 1B, bottom right; see *Methods*). In preliminary experiments, we photoactivated cells twice, first in early anaphase (Figure 1C, top) and then again between 4–6 min following the first activation (Figure 1C, bottom). In each of the six experiments, the half time for fluorescence dissipation increased (Figure 1D, top) and the velocity of microtubule sliding decreased from the first to second activation (Figure 1D, bottom) confirming work in other cell types demonstrating that microtubule dynamics and sliding are rapid in early anaphase (Vukušić *et al*., 2017; Yu *et al*., 2019) and are slower in late anaphase and telophase (Pamula *et al*., 2019). For these experiments images were collected at a 10–30-s interval and data were best fit with a single exponential (see *Methods*). This relatively long interval between images would not capture rapid events, so we next performed single activations at various times following AO using a 5-s interval between images. For the early anaphase cells, we observed the cells enter anaphase before photoactivation. For cells where time of AO was not observed, we estimated AO based on the

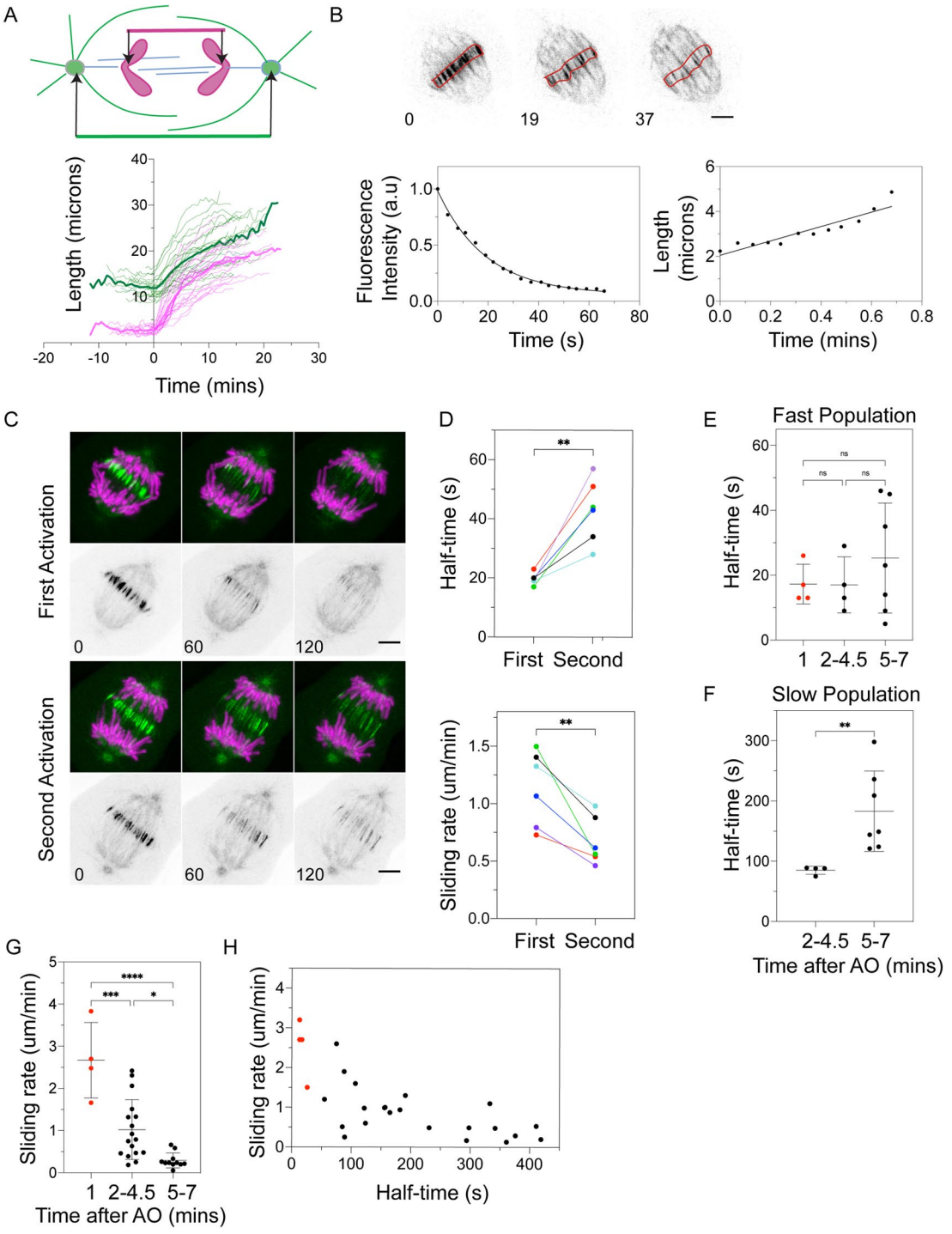

FIGURE 1: Gradual reduction in midzone microtubule turnover and sliding in anaphase. (A) Diagram of measurement of pole and chromosome distance (top). Chromosome–chromosome and pole-to-pole segregation in anaphase (bottom) (dark color, average; pale color, individual cells; $n = 15$ cells; Time 0 is AO). (B) Photoactivation of a representative anaphase cell (Top; red outline shows area used for measurement of dissipation); representative decay curve fitted to a single exponential decay (Bottom left, $R^2 = 0.99$). Length of photoactivated microtubules over time was plotted and fit to a linear regression to obtain sliding rate (bottom right). (C) Double photoactivation of a representative anaphase cell showing first activation (top two rows) and second activation (bottom two rows). Top rows: photoactivated microtubules (green) and DNA (magenta). Bottom rows: microtubules in grayscale. Bar = 5 µm. Time in s. (D) Plot of dissipation half time (top) and sliding rate (bottom) for the first and second activations. Each color is an individual cell ($n = 6$ cells). Plots of fluorescence dissipation (E and F) and sliding rate (G) for individual cells activated once at the indicated times following AO. Dissipation half times for fast (E) and slow (F) populations in individual cells activated once. (E) $n = 15$ cells; (F) $n = 11$ cells; (G) $n = 32$ cells; x-axis is time after AO. (H) Plot of dissipation half time for the more stable population vs. sliding rate; each dot is a single cell. Red dots are cells with only a single, fast half time. Statistical analysis (D) Paired *t* test; (E and G) ANOVA with the Tukey's post hoc test; (F) Mann-Whitney U test; *p* values: ns = $P > 0.12$; * = $P < 0.05$; ** = $p < 0.0021$; *** = $P < 0.0002$; **** = $P < 0.0001$.

average distance between the chromosomes at the time of photoactivation (Supplemental Figure 1A; see *Methods*).

When activations were performed within ~ 1 min of AO (red dots represent cells where AO was observed; Figure 1, E, G, and H), fluorescence dissipation was best fit by a single exponential (see *Methods*). The average half time of dissipation for early anaphase cells is 17± 6 s (mean ± SD; $n = 4$ cells; Figure 1E). When activations were performed during mid and late anaphase (2–4.5 and 5–7 min post AO, respectively), however, the data were best fit to a double exponential resulting in two half times (see *Methods*), indicative of two populations of microtubules with different dynamics. The fast phase had an average half time that was not different from the half time measured in the early anaphase cells (17 ± 9 s and 25 ± 17 s) for mid and late anaphase, respectively (Figure 1E). The less-dynamic population of microtubules had an average half time of 85 ± 9 s in midanaphase which increased to an average of 183 ± 67 s in late anaphase (Figure 1F).

As the midzone elongates, overlapping antiparallel microtubules slide relative to each other. To measure the dynamics of sliding, we quantified the distance that photoactivated marks on midzone microtubules moved (see *Methods*). The rate of sliding decreased from an average of 3 ± 0.9 μm/min in early anaphase to 1 ± 0.7 and 0.3 ± 0.2 μm/min in mid and late anaphase cells, respectively (Figure 1G; Pamula *et al.*, 2019). Comparison of sliding and turnover also showed that microtubules in early anaphase, which show rapid turnover, slide faster than microtubules in late anaphase (Figure 1H). In addition, the average rate of microtubule sliding in early anaphase is similar to the rate of chromosome motion but faster than the rate of pole-to-pole separation as observed in human cells (Supplemental Figure 1B; Vukušić *et al.*, 2017; Pamula *et al.*, 2019).

Midzone microtubule turnover during contractile ring ingression

Midzone microtubules provide signals which promote the assembly of an actomyosin ring at the equatorial cell cortex. Contraction of the ring causes ingression of a cleavage furrow which constrains components of the midzone into a focused structure called the midbody (Hu *et al.*, 2012; Peterman & Prekeris, 2019).

To examine midzone microtubule dynamics during cytokinesis in LLC-Pk1 cells, we first quantified furrowing in these cells. Cytokinetic ingression begins at an average of 9 ± 1 min after AO, and the furrow is approximately 50% ingressed by an average of 12 ± 2 min after AO (Figure 2A). Note that in these epithelial cells cleavage is asymmetric with the basal side completing furrowing before the apical side where cell–cell junctions are present, so the extent of furrowing was measured in the plane of the spindle toward the apical side (Higashi *et al.*, 2016).

To investigate microtubule turnover during cytokinesis, midzone microtubules were photoactivated and the percentage of ingression and the cell width at the equator were determined for each cell. As shown in Figure 2, midzone activations performed before ~50% ingression had measurable fluorescence dissipation and were categorized as dynamic (Figure 2B, top and 2C, black trace). In contrast, for cells with ~50% ingression, a half time could not be determined from the dissipation curve; microtubules in these cells were classified as static (Figure 2B, bottom and 2C, gray trace). For cells with ~50% ingression, the dissipation curve was best fit to a double exponential (Figure 2C, black trace). The half time for the fast population was not different from that measured in cells in early anaphase (average half time of 24 ± 30 s; $n = 6$ cells; Figure 2D bottom; see Figure 1E; Supplemental Figure 1C, left). The half time for the more stable microtubule population, however, was greater than that measured in late anaphase cells, demonstrating the continued stabilization of midzone microtubules over time (average half time of 305 ± 97 s; $n = 6$ cells; Figure 2, D, bottom, and E). Similar results were obtained when cell width was used to estimate the extent of ingression (Figure 2F). This data shows that the transition to a static array occurred when cell width is ~ 8 μm.

Midzone microtubule sliding was also measured during cytokinesis (Figure 2, G and H). Cells at ~50% ingression showed sliding at an average rate of 0.2 ± 0.07 μm/min, which was not statistically different from sliding in late-anaphase cells (Figure 2H). Sliding could not be detected in cells with >50% ingression (Figure 2G, bottom).

PRC1 and Kif4a regulate midzone microtubule turnover

Midzone formation requires the conserved microtubule binding protein PRC1 (Kurasawa *et al.*, 2004; Verbrugghe & White, 2004; Mollinari *et al.*, 2005; Zhu & Jiang, 2005). In metaphase and early anaphase PRC1 localizes to long stretches of antiparallel microtubules and is dynamic as measured by fluorescence recovery after photobleaching (FRAP) (Polak *et al.*, 2017; Asthana *et al.*, 2021). As anaphase progresses PRC1 and its binding partner Kif4a localize to short zones at the equator of the midzone (Kurasawa *et al.*, 2004; Mollinari *et al.*, 2005; Pamula *et al.*, 2019; Asthana *et al.*, 2021). This dynamic reorganization of PRC1/Kif4a ultimately acts to prevent further midzone elongation (Kurasawa *et al.*, 2004; Pamula *et al.*, 2019). To determine whether and how these midzone proteins impact midzone microtubule dynamics, we depleted each protein using siRNA (*Methods*; Supplemental Figure 2).

Kif4a and the centralspindlin subunit, MKLP1, were not detected in cells depleted of PRC1 (Supplemental Figure 2A), confirming the requirement for PRC1 to generate a robust midzone (Kurasawa *et al.*, 2004; Adriaans *et al.*, 2019; Pamula *et al.*, 2019).

We next examined microtubule dynamics in anaphase and cytokinesis cells following treatment with siRNA targeting PRC1. PRC1-depleted cells in anaphase lacked prominent microtubule bundles (Supplemental Figure 2B, left). Photoactivation of depleted cells 3–6 min post AO, showed a single population of highly dynamic microtubules. The average half time for these cells, 27 ± 10 s ($n = 4$ cells), was not different from that measured in control early anaphase cells (Supplemental Figure 2B, middle right). These data demonstrate that midzone microtubules in anaphase cells depleted of PRC1 remain as dynamic as microtubules in control cells in early anaphase. Next, we tested the contribution of PRC1 to midzone microtubule dynamics in cytokinesis cells at >50% ingression, a time when midzone microtubules in control cells have converted to a static array. These cells, we can also confirm that each cell is depleted by measuring the distance between the two nuclei (Supplemental Figure 2C, left; see *Methods*). In contrast to control cells, midzone microtubules in cells depleted of PRC1 at >50% ingression remained dynamic, and the dissipation curve was best fit by a double exponential (Figure 3, A and B, top). The faster population (average dissipation half time 16 ± 12 s; $n = 11$ cells; Figure 3C) was indistinguishable from the fast population of microtubules in control anaphase cells (Supplemental Figure 1C, left). The slower population had an average half time of 121 ± 72 s; $n = 11$ cells, which is like that observed in control cells during midanaphase (Supplemental Figure 1C, right). Sliding was not measured in these cells because the reduced number of microtubules in the midzone precluded accurate measurements.

One mechanism by which loss of PRC1 could impact midzone dynamics is through its binding partner, Kif4a, which suppresses microtubule plus-end elongation. Kif4a recruitment to the midzone by

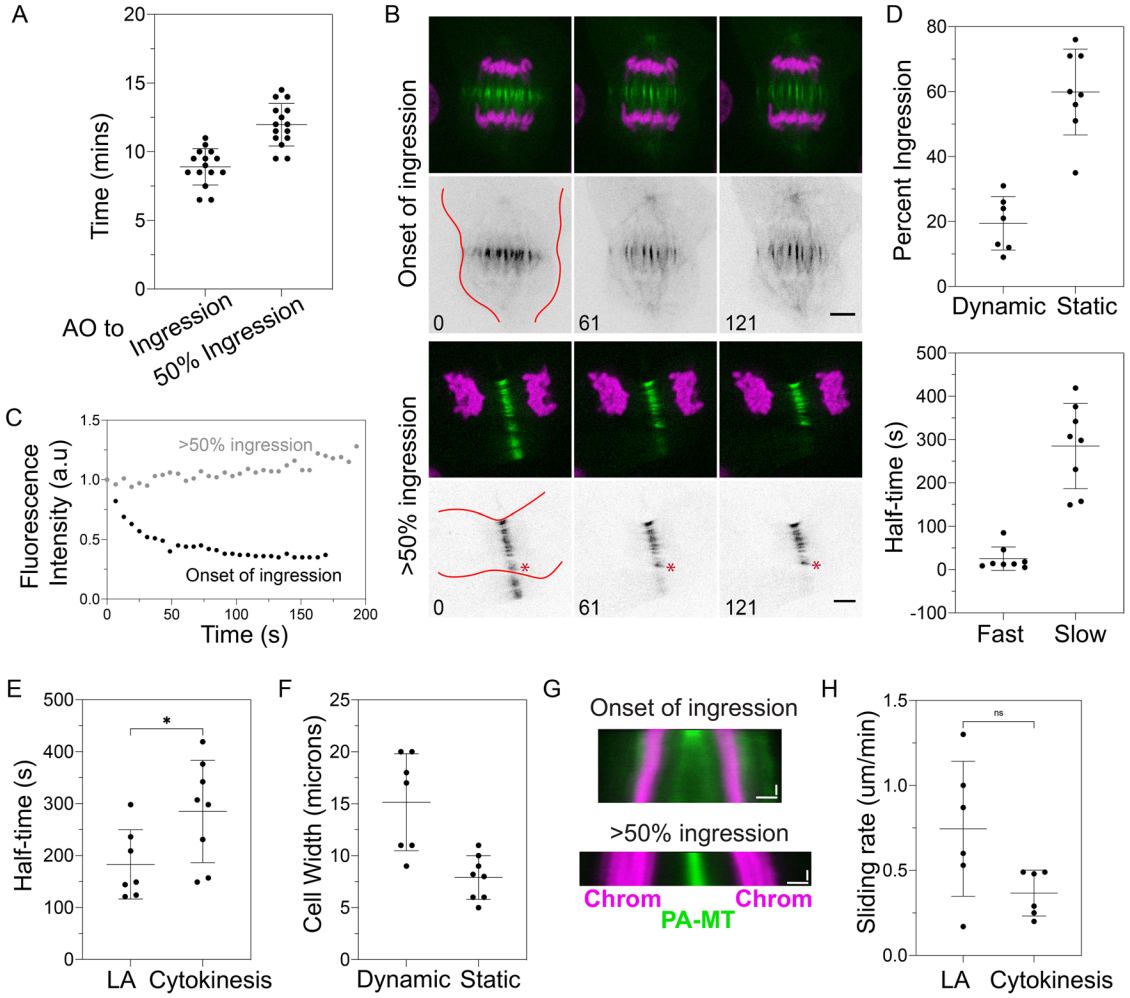

FIGURE 2: Microtubules transition from stable to static at midcytokinesis. (A) Time from AO to the onset of ingression and to 50% ingression ($n = 15$ cells). (B) Photoactivation of midzone microtubules at onset (top cell) and >50% ingression (bottom cell). Top rows: photoactivated microtubules (green) and DNA (magenta). Bottom rows: microtubules in grayscale. Bars = 5 μm. Cell edge outlined in red in first frame (top and bottom). Bottom panel red asterisk marks peripheral bundle; the area of activation extended into a neighboring cell (outside the red outline). Time in s. (C) Dissipation curves for representative cells photoactivated at onset (black) and after 50% ingression (gray). AU; arbitrary units of fluorescence; time in seconds. (D) (Top) cells were scored for dynamic or static microtubules and percentage of ingression was measured ($n = 15$ cells); (Bottom) half times of fluorescence dissipation for cytokinetic cells with dynamic microtubules ($n = 8$ cells). (E) Comparison of dissipation half time for the more stable population in late anaphase and cytokinesis ($n = 15$ cells). (F) Cells were scored for dynamic or static microtubules and cell width at the equator was measured ($n = 15$ cells). (G) Kymographs of chromosomes and photoactivated microtubules in cells photoactivated at the onset (top) and following 50% ingression (bottom); DNA in magenta, photoactivation zone in green. Vertical bar, time = 60 s; horizontal bar = 5 μm. (H) Plot of rate of microtubule sliding for cytokinetic cells at onset of ingression ($n = 6$ cells); LA (late anaphase 5–7 min post AO) shown for comparison. Statistical analysis (E) Mann-Whitney U test; p values: * = $P < 0.05$.

PRC1 regulates the length of antiparallel midzone microtubules both in vitro and in vivo (Bieling *et al.*, 2010; Hu *et al.*, 2011; Hannabuss *et al.*, 2019). Imaging of EGFP-α-tubulin expressing LLC-Pk1 cells depleted of Kif4a showed that midzone microtubules were frequently curved or buckled (Supplemental Figure 2C, middle); the distance between nuclei in telophase was greater and the microtubules were longer than in control cells (Supplemental Figure 2C, left, right). The length and lack of robust microtubule bundles in Kif4a-depleted cells is consistent with previous electron-microscopy observations (Hu *et al.*, 2011). Kif4a-depleted cells lack detectable Kif4a, by immunofluorescence (Supplemental Figure 2D) and have extended regions of PRC1 overlap zones (Supplemental Figure 2D; Figure 3, E and F) confirming that antiparallel microtubule overlap length is longer in depleted than in control cells. The majority of overlaps are likely composed of antiparallel microtubules; however, it has been shown that PRC1 can also decorate individual microtubules (Subramanian *et al.*, 2013).

First, we measured microtubule dynamics in Kif4a-depleted cells in anaphase. Given the variability of microtubule dynamics as anaphase progresses, we used sequential photoactivations in individual cells (see Figure 1, C and D), an approach that reveals whether microtubule dynamics change as cells progress through anaphase. Similar to the control cells, Kif4a-depleted cells were photoactivated twice, first in early anaphase and then again between 3–6 min following the first activation. In each of the control cells, microtubule turnover in anaphase slowed from the first to

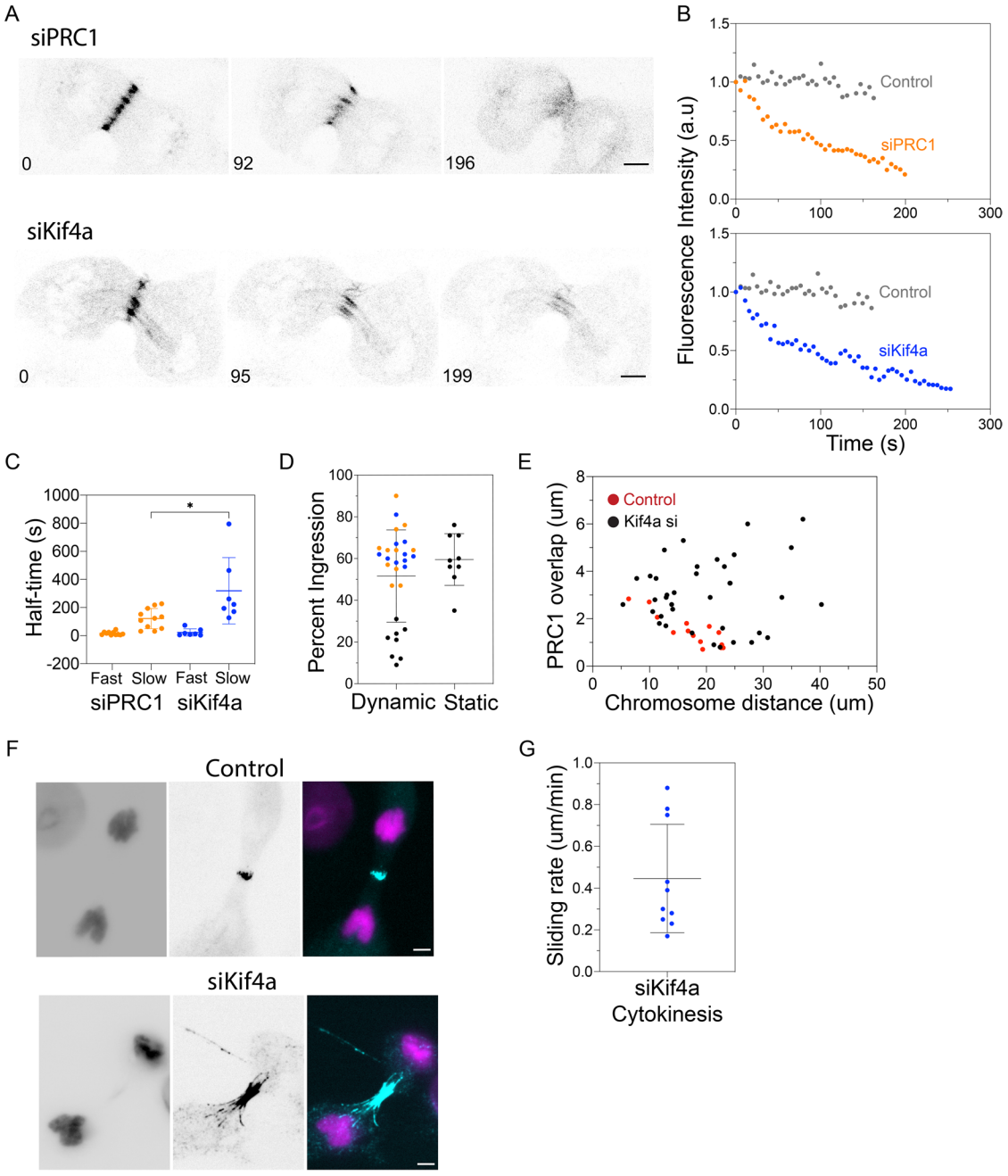

FIGURE 3: PRC1 and Kif4a impact microtubule stabilization in anaphase and telophase. (A) Photoactivation of cells depleted of PRC1 (top) and Kif4a (bottom) at >50% ingression. Bar = 5 μm. Time in s. (B) Dissipation curves for representative cells at >50% ingression, PRC1 (top, orange), and Kif4a depleted cells (bottom, blue). Dissipation for control at >50% ingression (gray) for comparison. (C) Plot of dissipation half times for PRC1 and Kif4a depleted cells at >50% ingression (PRC1 $n = 11$ cells; Kif4a $n = 7$ cells). (D) Cells were scored for dynamic or static microtubules and percentage of ingression for control (black), PRC1 (orange), and Kif4a (blue) depleted cells (control $n = 17$ cells; PRC1 $n = 11$ cells; Kif4a $n = 10$ cells; control cells from Figure 2E). (E) Plot of length of PRC1 overlap zone for control (red) and Kif4a depleted cells (black); Chr–Chr distance on x-axis. (F) Immunofluorescence staining for PRC1 in control (left) and Kif4a depleted cells (right); panels show DNA (left); PRC1 (middle); and merge with DNA in magenta and PRC1 in cyan (right). Bar = 5 μm. (G) Plot of rate of midzone sliding for Kif4a depleted cells at >50% ingression ($n = 10$ cells). Statistical analysis (C) Mann-Whitney U test; p values: * = $P < 0.05$.

second activation; in Kif4a-depleted cells, however, turnover was similar for the first and second activations (Supplemental Figure 2E). The rate of microtubule sliding was also measured in these cells. For control cells, the rate of sliding was faster in early anaphase and then decreased. However, the rate of sliding for Kif4a-depleted cells was not significantly different between the first and second activations (Supplemental Figure 2E; Vukušić *et al.*, 2021). These data show that the gradual reduction in turnover observed in control cells was not detected in Kif4a-depleted cells. In addition, the rate of microtubule sliding was generally faster consistent

with the retention of longer overlaps in the depleted cells (Figure 3G; Hu *et al.*, 2011; Pamula *et al.*, 2019).

Next, we performed photoactivations in Kif4a depleted cells at >50% ingression.

Dissipation curves were best fit with a double exponential with an average half time for fast population of 23 ± 27 s which was not different from the dynamic population in control cells during anaphase and early cytokinesis (Supplemental Figure 1C, left). The dissipation half time for the more stable microtubules in Kif4a-depleted cells (319 ± 236 s; $n = 7$ cells) was significantly greater than in PRC1 depleted cells (121 ± 72 s), likely due to the retention of PRC1 in Kif4a-depleted cells (Figure 3C, Supplemental 2D). Thus, as observed in PRC1 depleted cells, static microtubule arrays failed to form in telophase cells lacking Kif4a (Figure 3, A and B, bottom panels). Microtubule sliding in telophase cells depleted of Kif4a was like that observed in control cells during mid to late anaphase (Figure 1G and 3G).

Although static arrays did not form, both Kif4a- and PRC1-depleted cells did contain relatively stable microtubules in late anaphase and cytokinesis. In PRC1-depleted cells, this could arise due to incomplete depletion of PRC1 and/or additional midzone components that bind and bundle microtubules. Candidates for microtubule stabilization in the absence of PRC1 include CPC, CLASP1/2, and centralspindlin (Maiato *et al.*, 2003; Bratman & Chang, 2007; Davies *et al.*, 2015). In addition, microtubule compaction may promote stability via contractile ring constriction (Verma & Maresca, 2019; Hirsch *et al.*, 2022). In Kif4a-depleted cells, PRC1 is retained and is likely to contribute to microtubule stabilization, in addition to the previously mentioned factors that may additionally promote stabilization.

Contractile ring ingression impacts microtubule behavior in telophase

Our results demonstrate that midzone microtubules are gradually stabilized and ultimately rendered static as cells exit mitosis. In addition, our data show that formation of a narrow, tightly focused zone of microtubule overlap, marked by PRC1, contributes to microtubule stabilization in anaphase and is required for the formation of a static midzone array in telophase. Previous work showed that stabilization of midzone microtubules, measured by resistance to cold or nocodazole induced disassembly, required contractile ring ingression (Cimini *et al.*, 1998; Landino & Ohi, 2016). Our results demonstrate that when PRC1 is depleted, static arrays are not formed despite ingression. To explore whether and how constriction of the contractile ring impacts midzone dynamics, we inhibited contractile ring formation using latrunculin B (LatB) which binds and sequesters actin monomers (Spector *et al.*, 1983; Fujiwara *et al.*, 2018) or inhibited Rho-GTPase with C3 transferase to prevent activation of myosin and formins (Aktories *et al.*, 2005; Kanada *et al.*, 2009). Cells treated with LatB failed to ingress and an F-actin-containing contractile ring did not assemble at the equatorial cortex (Figure 4A; Kanada *et al.*, 2009). Microtubule distribution in LatB-treated cells revealed bundled microtubules in the center of the midzone like control cells (Figure 4A). In addition, a second population of microtubules, which we refer to as peripheral microtubules, was detected in the treated cells (Kanada *et al.*, 2009). These microtubules were located between the noningressed membrane and the more central region of the midzone; additionally, prominent astral arrays were present in most treated cells (Kanada *et al.*, 2009; Verma & Maresca, 2019). A similar distribution of F-actin and microtubules was observed in C3-treated cells.

For these experiments, cells were photoactivated in telophase, as marked by decondensed chromosomes, to ensure that cytokinesis had been inhibited. The results revealed distinct kinetics for central and peripheral microtubules (Figure 4B). The dissipation of fluorescence for peripheral microtubules in both C3 and LatB-treated cells was best fit with a single exponential, with half times for dissipation of 32 ± 19 s and 25 ± 9 s for C3 and LatB, respectively, which are not different from the fast population of microtubules in control anaphase cells (Figure 4B; Supplemental Figure 1C, left). In control anaphase cells, peripheral microtubules are occasionally observed (Rusan & Wadsworth, 2005) however, because these microtubules were of low abundance and present only transiently, photoactivation experiments were unsuccessful. Of note, in control cells, peripheral bundles are stabilized during ingression, showing behavior like the more centrally located microtubules (see bundle marked with asterisk in Figure 2B, bottom panel). Together, these results demonstrate that cells blocked in cytokinesis contain a population of peripheral microtubules which have dynamic behavior like microtubules in early anaphase cells (Supplemental Figure 1C, left).

The dynamic turnover of the central microtubules in cells blocked in cytokinesis was also determined. Fluorescence dissipation curves for central microtubules in LatB and C3-treated cells were best fit with a double exponential with dynamic and more stable populations (Figure 4B, bottom). The dynamic population had dissipation half times like those measured for control cells (see Supplemental Figure 1C). The values for the slow population of microtubules in the central region of LatB and C3-treated cells were like early- and late-anaphase control cells, respectively. The more stable population in C3-treated cells (368 ± 154 s; $n = 6$ cells) was highly variable and statistically different from LatB-treated cells (127 ± 25 s; $n = 6$ cells; Figure 4B, bottom panel). This difference is likely related to the duration of treatment with each inhibitor. Photoactivations in LatB-treated cells were performed within 30 min of drug addition, because longer incubations resulted in loss of adhesion and cell shape, precluding successful experiments. In contrast, inhibition of RhoA with C3 required longer incubations (see *Methods*) and cells selected for activation could have been blocked in telophase for up to several hours.

To gain insight into the organization of central and peripheral microtubules, the length of PRC1 zones was measured in C3 and LatB-treated cells. For both treatments, PRC1 zones on peripheral microtubules were longer than for central microtubules. The length of PRC1 zones on central microtubules were not different from control telophase cells (Figure 4C, right). Longer PRC1 zones on peripheral microtubules could result from PRC1 decorating individual, nonoverlapping microtubules or from longer antiparallel overlap zones. For both central and peripheral microtubules, PRC1 zones did not compact laterally but remained spaced apart (Figure 4C). Our experiments show that constriction of the contractile ring gathers and stabilizes peripheral microtubules in normal cytokinesis (see Figure 2B and 3F) and that in the absence of constriction, microtubules are retained in the peripheral regions, and fail to stabilize.

DISCUSSION

Our quantitative analysis of midzone microtubule-dynamic behavior demonstrates that midzone microtubules transition from a single, highly dynamic population to a mixture of dynamic and more stable microtubules as anaphase progresses. Furthermore, the more stable population becomes even less dynamic over time. These data are consistent with prior observations that measured the behavior of midzone microtubules in early anaphase using photoactivation of PA-EGFP-α-tubulin (Yu *et al.*, 2019; Vukušić *et al.*, 2021) and in late

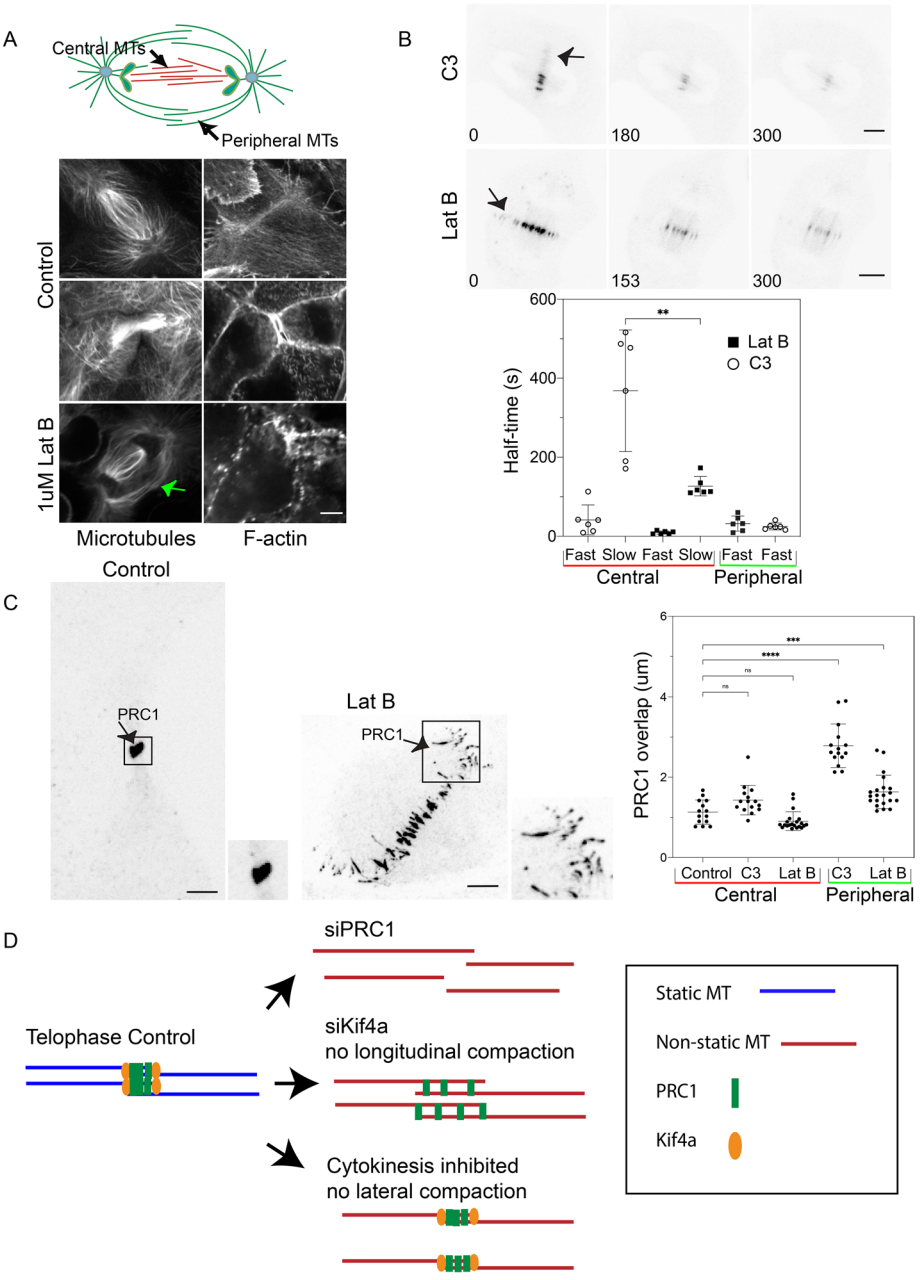

FIGURE 4: Transition to static microtubules requires lateral compaction of midzone microtubules in cytokinesis inhibited cells. (A) Diagram (top) showing peripheral and central midzone microtubules; (bottom) representative cells showing distribution of microtubules and F-actin in control cells in early and late cytokinesis (top two rows) and following treatment with Lat B (bottom). Left panels microtubules; right panels F-actin. Peripheral microtubules marked with green arrow. (B) Photoactivation of midzone microtubules in a representative telophase cell treated with C3 (top) or Lat B (bottom). Bar = 5 µm. Time in s. Peripheral microtubules marked with black arrows. (bottom) Plot of fluorescence dissipation half times for central (red line) and peripheral (green line) microtubules in C3 and LatB-treated cells (C3, $n = 6$ cells; LatB, $n = 6$ cells). (C) Immunofluorescence of PRC1 in the midzone of control cells (left) and LatB-treated cells (right) and graph of length of PRC1 for central (red line) and peripheral (green line) microtubules (Control, $n = 14$ cells; C3, $n = 15$ cells; Lat B, $n = 21$ cells). Higher magnification views of the region enclosed by the black box are shown on the right of control and the treated cell. (D) Diagram showing compaction of PRC1 in telophase control, PRC1-depleted cell (top), Kif4a-depleted cell (middle), and cytokinesis-inhibited cell (bottom). Statistical analysis (B) Mann-Whitney U test; (C) ANOVA with the Tukey's postdoc test; p values: ** = $p < 0.0021$; *** = $P < 0.0002$; **** = $P < 0.0001$.

anaphase and telophase cells using photobleaching of microinjected fluorescent tubulin (Saxton & McIntosh, 1987). The observation that the less-dynamic population of midzone microtubules became more stable as anaphase progressed is consistent with time-dependent modulation of microtubule dynamics as cells exit mitosis (Mollinari *et al.*, 2002; Neef *et al.*, 2007). Previous work showed that midzone microtubules are generated by augmin-mediated nucleation in the half-spindle and midzone regions (Goshima *et al.*, 2008; Uehara *et al.*, 2016; Štimac *et al.*, 2022; Trupinić *et al.*, 2022). Our results showing that dynamic microtubules are present throughout anaphase suggest that the augmin-dependent mechanism continually generates new, dynamic microtubules, as the half spindle shortens, and cells exit mitosis (Johmura *et al.*, 2011; Tsai *et al.*, 2011; Timón Pérez *et al.*, 2022; Zhang *et al.*, 2022). The final transition, from a mixture of stable and dynamic microtubules to a static array, occurred when cells reached ~ 50% ingression or a width of ~8 um and required compaction of the midzone microtubule bundles by the contractile ring.

Our results expand on prior work that used sensitivity to nocodazole or cold treatment to assess midzone microtubule stabilization as measured using nocodazole treatment (Landino & Ohi, 2016). The prior results showed that microtubules in postingression but not in preingression cells were resistant to disassembly, consistent with time-dependent stabilization (Hu *et al.*, 2011; Landino & Ohi, 2016). These experiments also showed that blocking ingression with either blebbistatin or cytochalasin prevented stabilization (Landino & Ohi, 2016). In contrast, we observed that stable microtubules were present when furrowing was blocked, but the final transition to a static array, for which no fluorescence dissipation could be measured, did not occur. One possible reason for this discrepancy is that photoactivation provides a quantitative measure of the extent of stabilization that is not revealed with high doses of nocodazole. Together our experiments and prior work demonstrate that across different cultured cells and in *Caenorhabditis elegans* midzone microtubules are gradually stabilized and then abruptly rendered static at ~ 50% ingression during telophase (Saxton & McIntosh, 1987; Yu *et al.*, 2019).

The results of these experiments support a model (Figure 4D) in which both

midzone proteins and cytokinesis drive the formation of a static array in telophase cells. In control cells, midzone microtubules in early anaphase are dynamic and transition to a mixture of dynamic and stable microtubules in midanaphase. Following ~ 50% cytokinetic ingression in telophase, midzone microtubules are converted to a static array for which no dissipation of fluorescence could be measured (blue microtubules in Figure 4D, telophase control, left panel). Cells depleted for PRC1 or Kif4a fail to form static arrays in telophase (red microtubules in Figure 4D, top right and middle), despite ingression and the concomitant formation of a bundle of microtubules. These cells either lack or have longitudinally expanded PRC1 zones (Figure 4D, top right and middle). This result demonstrates that longitudinally compacted zones of PRC1 are important for the transition to static microtubules. In addition, cells that fail to undergo cytokinetic ingression form stable, but not static, midzone microtubules. Although PRC1 and Kif4a are retained in these cells and undergo longitudinal compaction, these zones do not compact laterally (Figure 4D, bottom right). This data supports the possibility that contractile ring ingression forces neighboring bundles of midzone microtubules into close proximity, resulting in the formation of additional microtubule–microtubule crosslinks leading to increased stability (Mani *et al.*, 2021). The molecular mechanism by which this occurs is not yet understood; however, prior work has demonstrated that an interaction of the CPC subunit INCENP with actin contributes to midzone microtubule stability during ingression (Landino & Ohi, 2016).

In anaphase, both midzone and astral microtubules contribute signals that specify the location of contractile ring formation, although the former source has generally been considered more important in cultured mammalian cells (Cao & Wang, 1996; Wheatley, 1996). We observed a highly dynamic peripheral array of midzone microtubules in cells blocked in cytokinesis. Control cells also contained peripheral microtubules which were stabilized during furrow ingression (Verma & Maresca, 2019). These microtubules likely arise from nucleation at the centrosome, as astral arrays extending away from the equatorial region were also enhanced in these cells. The increase in microtubule elongation as cells exit mitosis may also contribute to the peripheral array (Rusan & Wadsworth, 2005). Recent work demonstrates that in *C. elegans* cells lacking a midzone, peripheral microtubules can form a midbody via contractile ring constriction (Hirsch *et al.*, 2022). Our experiments support the observation that multiple mechanisms can generate microtubules for midzone and midbody formation in telophase (Hirsch *et al.*, 2022).

Taken together our results quantify the dynamic parameters of midzone microtubules in mammalian cells from early anaphase to cytokinesis. The data show that dynamic microtubules are continually generated throughout anaphase and that these dynamic microtubules coexist with more stable microtubules. By ~50% ingression, midzone microtubules transition to a static array. Based on the timing of contractile ring ingression, we estimate that this final transition is accomplished within several minutes. The formation of a static array requires both longitudinal and lateral compaction of PRC1 on microtubules. Our results confirm that both PRC1 and Kif4a play critical roles in midzone formation in mammalian cells and reveal how cytokinesis impacts midzone microtubules, converting a stable array into a static structure.

MATERIAL AND METHODS

Request a protocol through *Bio-protocol*.

Materials unless otherwise stated, all reagents were obtained from Sigma-Aldrich.

Cell culture

Experiments were performed on LLC-Pk1 pig epithelial cells obtained from the ATCC and tested for mycoplasma. Cells were cultured in a 1:1 mixture of F-10 Hams and Opti-MEM (Thermo Fisher Scientific) containing 7.5% FBS (CPS Serum FBS-500-HI) and antibiotic–antimycotic. Cells were grown at 37°C and 5% CO2, in a humid atmosphere. In addition to parental cells, experiments were performed on LLC-Pk1 cells expressing EGFP-α tubulin or photoactivatable EGFP-α tubulin generated as previously described (Rusan *et al.*, 2001; Tulu *et al.*, 2003, 2010). For live-cell-imaging experiments, the growth medium was removed and replaced with non-CO_2 MEM medium lacking bicarbonate and containing HEPES. A temperature of ~37°C was maintained during imaging using either a Nicholson Precision Instruments Air stream stage incubator (Nicholson Precision Instruments ASI 400) or an Oko stage incubator (20/20 Technologies). Temperature was monitored using a thermistor probe adjacent to the culture dish (Air stream incubator) or within the heater (Oko).

Immunofluorescence

LLC-PK1 cells were plated on #1.5 22 × 22 mm coverslips 24–48 h before fixation. Cells were rinsed two or three times in room temperature calcium and magnesium free PBS, and then fixed in –20°C methanol for 4–10 min. Cells were rehydrated in PBS containing 0.1% Tween 20 and 0.02% Sodium Azide (PBS-Tw-Az). For some antibodies, cells were fixed in freshly prepared 0.25% glutaraldehyde, 2% paraformaldehyde, and 0.5% Triton X100, prepared in PBS. Cells were incubated in the manufacturer's recommended dilution of primary antibody prepared with 2% BSA in PBS-Tw-Az. The following antibodies were used in these experiments: PRC1 (Santa Cruz, 1:40), Kif4a (Santa Cruz,1:500), MKLP1 (Santa Cruz, 1:25), and tubulin (mouse anti-tubulin Dm1α [Sigma] 1:500) or sheep anti-tubulin (Cytoskeleton, 1:250).

Incubations with primary antibodies were performed in a humid chamber for 60 min at 37°C or overnight at room temperature. Coverslips were rinsed by dunking the coverslip at least 30 times in a beaker containing PBS-Tw-Az. Secondary antibody incubations were performed in a humid chamber at room temperature for 45 min, at the manufacturers recommended dilution, followed by rinsing as described above.

Coverslips were mounted in a mounting medium (Southern Biotech) containing DAPI and sealed with nail polish. The following secondary antibodies were used: Alexa Fluor 568 goat anti-mouse (Molecular Probes); Cy3 goat anti-rabbit (Jackson ImmunoResearch); Alexa Fluor 488 donkey anti-sheep (Jackson ImmunoResearch). F-Actin was visualized using rhodamine labeled phalloidin according to the manufacturer's recommended dilution (Molecular Probes). Cells stained with phalloidin were fixed in paraformaldehyde-glutaraldehyde as described above.

siRNA

For protein depletions, LLC-Pk1 cells (parental, or cells expressing EGFP-α tubulin or PA-EGFP-α tubulin) were plated at a density of 250,000 cells per well of a 12-well plate. The following day, cells were incubated with siRNA using Lipofectamine RNAiMax Transfection reagent (Invitrogen) according to the manufacturers' recommendations. All siRNAs were obtained from Sigma-Aldrich; siRNA was resuspended in RNAi buffer (Dharmacon) to a concentration of 100 μM. The final working concentration was 500 nM for PRC1 siRNA and 250 nM for Kif4a siRNA. Cells were incubated with siRNA for 5 h. After the 5-h incubation, cells were trypsinized and replated on either glass bottom dishes (MatTek Corp.) or on glass coverslips.

The sequences used for siRNA are: Kif4a 5'GCAGAUUGAAAGCCUAGAG3'; PRC1 5'UUGGGAUUCCAGAGGACCA3'.

Transfection efficiency was monitored using SiGLO (Dharmacon); control transfections contained all reagents but no siRNA.

Inhibitors

C3 transferase was obtained from Cytoskeleton (CT03) and rehydrated in distilled water to a concentration of 1 mg/ml and stored at −80°C. Immediately before use, C3 was prepared in a culture medium lacking serum to a final concentration of 4 ug/ml; cells were rinsed in PBS and then incubated with C3 for ~5 h at 37°C in a humid atmosphere.

Imaging

LLC-Pk1 cells expressing EGFP-α tubulin were imaged using a Nikon Ti-E microscope with a CSU-X1 Yokogawa Spinning disk confocal scan head and a 100X/NA1.4 oil immersion objective. Image acquisition was controlled by Metamorph software (Molecular Devices, LLC). Live cells were imaged with a 30–60 s or 2–4 min interval depending on the experiment. For imaging of fixed cells, complete Z-stacks were collected using a 0.30 µm spacing; exposure time varied depending on the antibody.

Photoactivations were performed on both a Spinning Disc and Resonant Scanning Confocal using Nikon Elements software. Photoactivation was performed after AO, perpendicular to the spindle long axis, in between separating chromatids, visualized with mCherry H2B or by differential interference contrast (DIC) optics. The stimulation type used was a line with a width of 1 pixel.

The scanning confocal system consisted of a Nikon Ti Microscope with A1HD Resonant Scanning Confocal with Galvano scanner and DU4 detector. An APO 60X/1.4NA oil immersion objective and a stage top incubator system (Okolab) was used. Photoactivation of PA-EGFP-α tubulin, a 405-nm laser was used. For all experiments the duration of pulse was set to 100 ms with no delay with laser power at 10.2%. PA- EGFP fluorescence was imaged using a 488-nm laser at 1.7% laser power, and H2B mCherry chromosomes were visualized using a 561-nm laser at 1.3% laser power. For majority of experiments, images were acquired at 5-s intervals. At each interval, three Z-slices at 1-µm spacing were acquired.

The spinning disk system consisted of a Nikon Ti Microscope with a Yokogawa Spinning Disc Confocal and Andor DU-897 camera. An APO VC 100X/1.4 oil immersion objective and stage top incubator system (Okolab) was used. For photoactivation of PA-EGFP-α tubulin, a 405-nm laser at 50% laser power for a duration pulse of 100 ms with no delay was used for all experiments. PA-EGFP fluorescence was imaged using a 488-nm laser with exposure of 300 ms and chromosomes were visualized using a 561-nm laser with exposure of 500 ms. Images were acquired at 10–30-s intervals.

Double-photoactivation experiments were performed similarly, using a Nikon A1R Resonant Scanning Confocal microscope with an APO 60X/1.4NA oil immersion objective. The stimulation type used was a rectangle with length of 16.6 µm and width of 0.6 µm. For this instrument the following laser settings were used: 405-nm laser 20.8%, 488-nm laser 2%, and 561-nm laser at 0.5%. Images were acquired every 30-s intervals. At each interval, three Z-slices at 1-µm spacing were acquired. Since performing these experiments, the 405-nm laser has been changed on the scanning confocal system.

Data and image analysis

To quantify fluorescence dissipation following photoactivation, we measured pixel intensities within an area drawn around the activated region for each cell using the freehand tool in FIJI (ImageJ open-source software). The Z-stacks were converted to sum projections for measurements. For each time point, a new area was drawn because the area occupied by the activated microtubules changes. The photoactivation or background area was never drawn on the chromosome region. The mean background intensity was taken within the spindle outside of the area containing activated microtubules for each frame. The mean fluorescence intensity values were multiplied by the area to obtain the integrative intensity for each time point. The same area value was used to calculated integrative intensity for the background. To determine how much photoactivable α tubulin fluorescence was lost, we divided the integrative values of the photoactivable α tubulin by the integrative values of the background and subtracted 1 from the ratio (Bailey *et al.*, 2015). The integrative fluorescence values were normalized to the first time point after photoactivation for each cell and fitted using Kaleidagraph (Kaleidagraph, Version 4.5 for MacOS. Synergy, Reading, PA. www.synergy.com). The plots of the fluorescence intensity as a function of time for the early anaphase cells were fit to a single exponential decay of the form: $x(t) = X\infty + A*\exp(-t/tau)$, where $X\infty$ is the offset, A is the amplitude, and tau is the characteristic decay time. All other cells were fit to a double exponential decay of the form: $x(t) = A*\exp(-t/tau_1) + B*\exp(-t/tau_2)$, where A and B represent the fast and slow microtubule population amplitudes, and tau_1 and tau_2 are the fast and slow timescales for the motion. For each fit, we recorded the goodness of the fit (R^2). The half time was determined by multiplying by the ln (2) by the characteristic time.

To determine sliding rates, the length of the photoactivation region was measured for each cell. The length of photoactivated spindle midzone was measured using FIJI by drawing a line segment along the photoactivated region across time points. Multiple bundles were tracked and averaged per frame. The length was plotted as a function of time on Prism (GraphPad Prism version 9.4.1 for MacOS, GraphPad Software, San Diego, CA, www.graphpad.com). The measurements were taken only for time points where the photoactivated bundles were clearly visible. A linear regression was performed on each curve for each individual cell. The sliding rates were calculated from the slope of a regression line. For cytokinesis cells at >50% ingression, sliding rates could not be determined as the change over time was smaller than our resolution.

The time of AO for each individual cell was defined as the time point immediately before the separation of sister chromatids. For some cells in which the time of AO was not observed, we estimated AO as follows: The average distance between the chromosomes was obtained at 30 s intervals for 10 mitotic cells and divided in two. The data was normalized for AO at time zero and the data was fit to an exponential rise. The equation $y = m2\text{^}(1-\exp(-m3*x))$ was simplified to $c2 = (-1/m3 * \ln (1-c3/m2)$ and was used to calculate time from distance. We then compared cells with known times of AO with calculated time and fitted the plot to a simple linear-regression curve fit (Supplemental Figure 1A).

Measurements were performed in FIJI and statistical analysis was performed in Prism (GraphPad Prism version 9.4.1 for MacOS, GraphPad Software, San Diego, CA, www.graphpad.com). The length of midzone microtubules in Kif4a-depleted cells was measured on a single z- plane of EGFP-α tubulin anaphase spindles, using the segmented line tool in FIJI. To measure the length of the PRC1 overlap zone, images were analyzed using either Metamorph software or FIJI. Individual slices of complete Z-stacks of stained cells were measured, and the average length of the overlap was determined for each cell. PRC1 overlap was plotted as a function of the length between the segregating chromosomes, measured using

the center of the DNA masses. For inhibited cells, only overlap zones in cells with reformed nuclear envelopes were measured. The time from AO to onset of furrowing and to 50% ingression was determined from movies of cells expressing EGFP-α tubulin. To quantify cell width and percent of ingression, the width of the cell before onset of ingression was measured, or in some cases estimated by fitting a curved line along the sides of the cell. Next the width was measured at the time of activation and the fraction of the initial width to the width at activation was determined. Measurements were performed using FIJI.

Images were assembled in Adobe Illustrator (Adobe, version 25.4.6. Adobe Illustrator).

Statistical analysis

Graphs of the data and statistical analysis were compiled using Prism (GraphPad Prism version 9.4.1 for MacOS, GraphPad Software, San Diego, CA, www.graphpad.com).

ACKNOWLEDGMENTS

The authors thank Dr. T. Maresca for insightful comments on this work. Dr. K. Velle provided editorial comments on the manuscript, and advice on Prism software. We thank Ms. Louiza Tizi-Ougdal and Eylen Diaz Soto for excellent assistance in the lab; Ms. Amanda Shorey for collecting preliminary data on protein depletions and experiments with Latrunculin. We especially thank Ms. Heather M. Jordan, a former master's student, whose work helped pave the way for this study. Photoactivations were performed in the Light Microscopy Facility and Nikon Center of Excellence at the Institute for Applied Life Sciences, University of Massachusetts Amherst, with the support from the Massachusetts Life Science Center. Funding was obtained from National Science Foundation MCB 2134215 and C.F.R. was supported by Soft Materials for Life Sciences National Research Traineeship Program 1545399 and the Spaulding-Smith STEM Fellowship.

REFERENCES

Adriaans IE, Basant A, Ponsioen B, Glotzer M, Lens SMA (2019). PLK1 plays dual roles in centralspindlin regulation during cytokinesis. J Cell Biol 218, 1250–1264.

Aher A, Kok M, Sharma A, Rai A, Olieric N, Rodriguez-Garcia R, Katrukha EA, Weinert T, Olieric V, Kapitein LC, *et al*. (2018). CLASP suppresses microtubule catastrophes through a single TOG domain. Dev Cell 46, 40–58.e8.

Aist JR, Bayles CJ, Tao W, Berns MW (1991). Direct experimental evidence for the existence, structural basis and function of astral forces during anaphase B in vivo. J Cell Sci 100, 279–288.

Aist JR, Liang H, Berns MW (1993). Astral and spindle forces in PtK2 cells during anaphase B: A laser microbeam study. J Cell Sci 104, 1207–1216.

Aktories K, Wilde C, Vogelsgesang M (2005). Rho-modifying C3-like ADP-ribosyltransferases. In: Reviews of Physiology, Biochemistry and Pharmacology, Heidelberg, Berlin: Springer, 1–22. https://doi.org/10.1007/s10254-004-0034-4

Al-Bassam J, Kim H, Brouhard G, van Oijen A, Harrison SC, Chang F (2010). CLASP promotes microtubule rescue by recruiting tubulin dimers to the microtubule. Dev Cell 19, 245–258.

Alsop GB, Zhang D (2003). Microtubules are the only structural constituent of the spindle apparatus required for induction of cell cleavage. J Cell Biol 162, 383–390.

Alsop GB, Zhang D (2004). Microtubules continuously dictate distribution of actin filaments and positioning of cell cleavage in grasshopper spermatocytes. J Cell Sci 117, 1591–1602.

Asthana J, Cade NI, Normanno D, Lim WM, Surrey T (2021). Gradual compaction of the central spindle decreases its dynamicity in PRC1 and EB1 gene-edited cells. Life Sci Alliance 4, e202101222.

Bailey ME, Sackett DL, Ross JL (2015). Katanin severing and binding microtubules are inhibited by tubulin carboxy tails. Biophys J 109, 2546–2561.

Bieling P, Telley IA, Surrey T (2010). A minimal midzone protein module controls formation and length of antiparallel microtubule overlaps. Cell 142, 420–432.

Bratman SV, Chang F (2007). Stabilization of overlapping microtubules by fission yeast CLASP. Dev Cell 13, 812–827.

Brust-Mascher I, Scholey JM (2011). Mitotic motors and chromosome segregation: The mechanism of anaphase B. Biochemical Soc Trans 39, 1149–1153.

Cande WZ, McDonald KL (1985). In vitro reactivation of anaphase spindle elongation using isolated diatom spindles. Nature 316, 168–170.

Canman JC, Lewellyn L, Laband K, Smerdon SJ, Desai A, Bowerman B, Oegema K (2008). Inhibition of Rac by the GAP activity of centralspindlin is essential for cytokinesis. Science 322, 1543–1546.

Cao LG, Wang YL (1996). Signals from the spindle midzone are required for the stimulation of cytokinesis in cultured epithelial cells. Mol Biol Cell 7, 225–232.

Cimini D, Fioravanti D, Tanzarella C, Degrassi F (1998). Simultaneous inhibition of contractile ring and central spindle formation in mammalian cells treated with cytochalasin B. Chromosoma 107, 479–485.

Collins E, Mann BJ, Wadsworth P (2014). Eg5 restricts anaphase B spindle elongation in mammalian cells. Cytoskeleton (Hoboken) 71, 136–144.

Davies T, Kodera N, Kaminski Schierle GS, Rees E, Erdelyi M, Kaminski CF, Ando T, Mishima M (2015). CYK4 promotes antiparallel microtubule bundling by optimizing MKLP1 neck conformation. PLoS Biol 13, e1002121.

Fujiwara I, Zweifel ME, Courtemanche N, Pollard TD (2018). Latrunculin A accelerates actin filament depolymerization in addition to sequestering actin monomers. Curr Biol 28, 3183–3192.e2.

Gaska I, Armstrong ME, Alfieri A, Forth S (2020). The mitotic crosslinking protein PRC1 acts like a mechanical dashpot to resist microtubule sliding. Dev Cell 54, 367–378.e5.

Glotzer M (2009). The 3Ms of central spindle assembly: microtubules, motors and MAPs. Nat Rev Mol Cell Biol 10, 9–20.

Goshima G, Mayer M, Zhang N, Stuurman N, Vale RD (2008). Augmin: a protein complex required for centrosome-independent microtubule generation within the spindle. J Cell Biol 181, 421–429.

Grill SW, Howard J, Schäffer E, Stelzer EHK, Hyman AA (2003). The distribution of active force generators controls mitotic spindle position. Science 301, 518–521.

Grill SW, Hyman AA (2005). Spindle positioning by cortical pulling forces. Dev Cell 8, 461–465.

Hannabuss J, Lera-Ramirez M, Cade NI, Fourniol FJ, Nédélec F, Surrey T (2019). Self-organization of minimal anaphase spindle midzone bundles. Curr Biol 29, 2120–2130.e7.

Heald R, Khodjakov A (2015). Thirty years of search and capture: the complex simplicity of mitotic spindle assembly. J Cell Biol 211, 1103–1111.

Higashi T, Arnold TR, Stephenson RE, Dinshaw KM, Miller AL (2016). Maintenance of the epithelial barrier and remodeling of cell-cell junctions during cytokinesis. Curr Biol 26, 1829–1842.

Hirose K, Kawashima T, Iwamoto I, Nosaka T, Kitamura T (2001). MgcRacGAP is involved in cytokinesis through associating with mitotic spindle and midbody. J Biol Chem 276, 5821–5828.

Hirsch SM, Edwards F, Shirasu-Hiza M, Dumont J, Canman JC (2022). Functional midbody assembly in the absence of a central spindle. J Cell Biol 221, e202011085.

Hu C-K, Coughlin M, Field CM, Mitchison TJ (2011). KIF4 regulates midzone length during cytokinesis. Curr Biol 21, 815–824.

Hu C-K, Coughlin M, Mitchison TJ (2012). Midbody assembly and its regulation during cytokinesis. Mol Biol Cell 23, 1024–1034.

Hutterer A, Glotzer M, Mishima M (2009). Clustering of centralspindlin is essential for its accumulation to the central spindle and the midbody. Curr Biol 19, 2043–2049.

Jagrić M, Risteski P, Martinčić J, Milas A, Tolić IM (2021). Optogenetic control of PRC1 reveals its role in chromosome alignment on the spindle by overlap length-dependent forces. Elife 10, e61170.

Janson ME, Loughlin R, Loïodice I, Fu C, Brunner D, Nédélec FJ, Tran PT (2007). Crosslinkers and motors organize dynamic microtubules to form stable bipolar arrays in fission yeast. Cell 128, 357–368.

Jantsch-Plunger V, Gönczy P, Romano A, Schnabel H, Hamill D, Schnabel R, Hyman AA, Glotzer M (2000). Cyk-4: A Rho family gtpase activating protein (Gap) required for central spindle formation and cytokinesis. J Cell Biology 149, 1391–1404.

Johmura Y, Soung N-K, Park J-E, Yu L-R, Zhou M, Bang JK, Kim B-Y, Veenstra TD, Erikson RL, Lee KS (2011). Regulation of microtubule-based microtubule nucleation by mammalian polo-like kinase 1. Proc Natl Acad Sci USA 108, 11446–11451.

Kanada M, Nagasaki A, Uyeda TQP (2009). Stabilization of anaphase midzone microtubules is regulated by Rho during cytokinesis in human fibrosarcoma cells. Exp Cell Res 315, 2705–2714.
Kapitein LC, Janson ME, van den Wildenberg SMJL, Hoogenraad CC, Schmidt CF, Peterman EJG (2008). Microtubule-driven multimerization recruits ase1p onto overlapping microtubules. Curr Biol 18, 1713–1717.
Khodjakov A, La Terra S, Chang F (2004). Laser microsurgery in fission yeast: role of the mitotic spindle midzone in anaphase B. Curr Biol 14, 1330–1340.
Khodjakov A, Rieder CL (1999). The sudden recruitment of γ-Tubulin to the centrosome at the onset of mitosis and its dynamic exchange throughout the cell cycle, do not require microtubules. J Cell Biol 146, 585–596.
Kotak S, Busso C, Gönczy P (2014). NuMA interacts with phosphoinositides and links the mitotic spindle with the plasma membrane. EMBO J 33, 1815–1830.
Kurasawa Y, Earnshaw WC, Mochizuki Y, Dohmae N, Todokoro K (2004). Essential roles of KIF4 and its binding partner PRC1 in organized central spindle midzone formation. EMBO J 23, 3237–3248.
Laband K, Le Borgne R, Edwards F, Stefanutti M, Canman JC, Verbavatz J-M, Dumont J (2017). Chromosome segregation occurs by microtubule pushing in oocytes. Nat Commun 8, 1499.
Landino J, Ohi R (2016). The timing of midzone stabilization during cytokinesis depends on myosin II activity and an interaction between INCENP and actin. Curr Biol 26, 698–706.
Lee K-Y, Esmaeili B, Zealley B, Mishima M (2015). Direct interaction between centralspindlin and PRC1 reinforces mechanical resilience of the central spindle. Nat Commun 6, 7290.
Li F, Higgs HN (2003). The mouse formin mDia1 is a potent actin nucleation factor regulated by autoinhibition. Curr Biol 13, 1335–1340.
Liu J, Wang Z, Jiang K, Zhang L, Zhao L, Hua S, Yan F, Yang Y, Wang D, Fu C, *et al*. (2009). PRC1 cooperates with CLASP1 to organize central spindle plasticity in mitosis. J Biol Chem 284, 23059–23071.
Maiato H, Fairley EAL, Rieder CL, Swedlow JR, Sunkel CE, Earnshaw WC (2003). Human CLASP1 is an outer kinetochore component that regulates spindle microtubule dynamics. Cell 113, 891–904.
Maiato H, Gomes A, Sousa F, Barisic M (2017). Mechanisms of chromosome congression during mitosis. Biology (Basel) 6, 13.
Maiato H, Lince-Faria M (2010). The perpetual movements of anaphase. Cell Mol Life Sci 67, 2251–2269.
Mani N, Jiang S, Neary AE, Wijeratne SS, Subramanian R (2021). Differential regulation of single microtubules and bundles by a three-protein module. Nat Chem Biol 17, 964–974.
Mastronarde DN, McDonald KL, Ding R, McIntosh JR (1993). Interpolar spindle microtubules in PTK cells. J Cell Biol 123, 1475–1489.
Maton G, Edwards F, Lacroix B, Stefanutti M, Laband K, Lieury T, Kim T, Espeut J, Canman JC, Dumont J (2015). Kinetochore components are required for central spindle assembly. Nat Cell Biol 17, 697–705.
Matsumura F (2005). Regulation of myosin II during cytokinesis in higher eukaryotes. Trends Cell Biol 15, 371–377.
McIntosh JR (2017). Assessing the contributions of motor enzymes and microtubule dynamics to mitotic chromosome motions. Annu Rev Cell Dev Biol 33, 1–22.
McIntosh JR, Molodtsov MI, Ataullakhanov FI (2012). Biophysics of mitosis. Q Rev Biophys 45, 147–207.
Mishima M, Lee K-Y (2015). Central spindle robustness by PRC1-centralspindlin interaction. Cell Cycle 14, 3515–3516.
Mollinari C, Kleman J-P, Jiang W, Schoehn G, Hunter T, Margolis RL (2002). PRC1 is a microtubule binding and bundling protein essential to maintain the mitotic spindle midzone. J Cell Biol 157, 1175–1186.
Mollinari C, Kleman J-P, Saoudi Y, Jablonski SA, Perard J, Yen TJ, Margolis RL (2005). Ablation of PRC1 by small interfering RNA demonstrates that cytokinetic abscission requires a central spindle bundle in mammalian cells, whereas completion of furrowing does not. Mol Biol Cell 16, 1043–1055.
Neef R, Gruneberg U, Kopajtich R, Li X, Nigg EA, Sillje H, Barr FA (2007). Choice of Plk1 docking partners during mitosis and cytokinesis is controlled by the activation state of Cdk1. Nat Cell Biol 9, 436–444.
Nishimura Y, Yonemura S (2006). Centralspindlin regulates ECT2 and RhoA accumulation at the equatorial cortex during cytokinesis. J Cell Sci 119, 104–114.
Nunes Bastos R, Gandhi SR, Baron RD, Gruneberg U, Nigg EA, Barr FA (2013). Aurora B suppresses microtubule dynamics and limits central spindle size by locally activating KIF4A. J Cell Biol 202, 605–621.
Pamula MC, Carlini L, Forth S, Verma P, Suresh S, Legant WR, Khodjakov A, Betzig E, Kapoor TM (2019). High-resolution imaging reveals how the spindle midzone impacts chromosome movement. J Cell Biol 218, 2529–2544.
Peterman E, Prekeris R (2019). The postmitotic midbody: regulating polarity, stemness, and proliferation. J Cell Biol 218, 3903–3911.
Polak B, Risteski P, Lesjak S, Tolić IM (2017). PRC 1-labeled microtubule bundles and kinetochore pairs show one-to-one association in metaphase. EMBO Rep 18, 217–230.
Roostalu J, Schiebel E, Khmelinskii A (2010). Cell cycle control of spindle elongation. Cell Cycle 9, 1084–1090.
Rusan NM, Fagerstrom CJ, Yvon A-MC, Wadsworth P (2001). Cell cycle-dependent changes in microtubule dynamics in living cells expressing green fluorescent protein-α tubulin. Mol Biol Cell 12, 971–980.
Rusan NM, Wadsworth P (2005). Centrosome fragments and microtubules are transported asymmetrically away from division plane in anaphase. J Cell Biol 168, 21–28.
Saunders AM, Powers J, Strome S, Saxton WM (2007). Kinesin-5 acts as a brake in anaphase spindle elongation. Curr Biol 17, R453–R454.
Saxton WM, McIntosh JR (1987). Interzone microtubule behavior in late anaphase and telophase spindles. J Cell Biol 105, 875–886.
Spector I, Shochet NR, Kashman Y, Groweiss A (1983). Latrunculins: novel marine toxins that disrupt microfilament organization in cultured cells. Science 219, 493–495.
Steblyanko Y, Rajendraprasad G, Osswald M, Eibes S, Jacome A, Geley S, Pereira AJ, Maiato H, Barisic M (2020). Microtubule poleward flux in human cells is driven by the coordinated action of four kinesins. EMBO J 39. e105432. https://doi.org/10.15252/embj.2020105432
Štimac V, Koprivec I, Manenica M, Simunić J, Tolić IM (2022). Augmin prevents merotelic attachments by promoting proper arrangement of bridging and kinetochore fibers. Elife 11, e83287.
Stumpff J, Wagenbach M, Franck A, Asbury CL, Wordeman L (2012). Kif18A and chromokinesins confine centromere movements via microtubule growth suppression and spatial control of kinetochore tension. Dev Cell 22, 1017–1029.
Subramanian R, Ti S-C, Tan L, Darst SA, Kapoor TM (2013). Marking and measuring single microtubules by PRC1 and Kinesin-4. Cell 154, 377–390.
Subramanian R, Wilson-Kubalek EM, Arthur CP, Bick MJ, Campbell EA, Darst SA, Milligan RA, Kapoor TM (2010). Insights into antiparallel microtubule crosslinking by PRC1, a conserved nonmotor microtubule binding protein. Cell 142, 433–443.
Timón Pérez K, Scrofani J, Vernos I (2022). NEDD1-S411 phosphorylation plays a critical function in the coordination of microtubule nucleation during mitosis. Biol Open 11, bio059474.
Trupinić M, Kokanović B, Ponjavić I, Barišić I, Šegvić S, Ivec A, Tolić IM (2022). The chirality of the mitotic spindle provides a mechanical response to forces and depends on microtubule motors and augmin. Curr Biol 32, 2480–2493.e6.
Tsai CY, Ngo B, Tapadia A, Hsu P-H, Wu G, Lee W-H (2011). Aurora-A phosphorylates augmin complex component hice1 protein at an N-terminal serine/threonine cluster to modulate its microtubule binding activity during spindle assembly. J Biol Chem 286, 30097–30106.
Tulu US, Ferenz NP, Wadsworth P (2010). Photoactivatable green fluorescent protein-tubulin. Methods Cell Biol 286, 81–90.
Tulu US, Rusan NM, Wadsworth P (2003). Peripheral, non-centrosome-associated microtubules contribute to spindle formation in centrosome-containing cells. Curr Biol 13, 1894–1899.
Uehara R, Kamasaki T, Hiruma S, Poser I, Yoda K, Yajima J, Gerlich DW, Goshima G (2016). Augmin shapes the anaphase spindle for efficient cytokinetic furrow ingression and abscission. Mol Biol Cell 27, 812–827.
Uehara R, Nozawa R, Tomioka A, Petry S, Vale RD, Obuse C, Goshima G (2009). The augmin complex plays a critical role in spindle microtubule generation for mitotic progression and cytokinesis in human cells. Proc Natl Acad Sci 106, 6998–7003.
Verbrugghe KJC, White JG (2004). SPD-1 Is required for the formation of the spindle midzone but is not essential for the completion of cytokinesis in C. elegans embryos. Curr Biol 14, 1755–1760.
Verma V, Maresca TJ (2019). Microtubule plus-ends act as physical signaling hubs to activate RhoA during cytokinesis. Elife 8, e38968.
Vernì F, Somma MP, Gunsalus KC, Bonaccorsi S, Belloni G, Goldberg ML, Gatti M (2004). Feo, the Drosophila homolog of PRC1, is required for central-spindle formation and cytokinesis. Curr Biol 14, 1569–1575.

Vukušić K, Buđa R, Bosilj A, Milas A, Pavin N, Tolić IM (2017). Microtubule sliding within the bridging fiber pushes kinetochore fibers apart to segregate chromosomes. Dev Cell 43, 11–23.e6.
Vukušić K, Buđa R, Tolić IM (2019). Force-generating mechanisms of anaphase in human cells. J Cell Sci 132, jcs231985.
Vukušić K, Ponjavić I, Buđa R, Risteski P, Tolić IM (2021). Microtubule-sliding modules based on kinesins EG5 and PRC1-dependent KIF4A drive human spindle elongation. Dev Cell 56, 1253–1267.e10.
Vukušić K, Tolić IM (2021). Anaphase B: Long-standing models meet new concepts. Semin Cell Dev Biol 117, 127–139.
Wheatley SP (1996). Midzone microtubule bundles are continuously required for cytokinesis in cultured epithelial cells [correction published in J Cell Biol(1996). 135, 1679]. J Cell Biol 135, 981–989.
Wijeratne S, Subramanian R (2018). Geometry of antiparallel microtubule bundles regulates relative sliding and stalling by PRC1 and Kif4A. Elife 7, e32595.
Yu C-H, Redemann S, Wu H-Y, Kiewisz R, Yoo TY, Conway W, Farhadifar R, Müller-Reichert T, Needleman D (2019). Central-spindle microtubules are strongly coupled to chromosomes during both anaphase A and anaphase B. Mol Biol Cell 30, 2503–2514.
Zhang Y, Hong X, Hua S, Jiang K (2022). Reconstitution and mechanistic dissection of the human microtubule branching machinery. J Cell Biol 221, e202109053.
Zhu C, Jiang W (2005). Cell cycle-dependent translocation of PRC1 on the spindle by Kif4 is essential for midzone formation and cytokinesis. Proc Natl Acad Sci USA 102, 343–348.